

DuoSpaceNet: Leveraging Both Bird’s-Eye-View and Perspective View Representations for 3D Object Detection

Zhe Huang*
zhuang334@wisc.edu

Yizhe Zhao*
yiz086@ucsd.edu

Hao Xiao
alexinu@uw.edu

Chenyan Wu
czw390@psu.edu

Lingting Ge
gelingting@gmail.com

Abstract

Recent advances in multi-view camera-only 3D object detection either rely on an accurate reconstruction of bird’s-eye-view (BEV) 3D features or on traditional 2D perspective view (PV) image features. While both have their own pros and cons, few have found a way to stitch them together in order to benefit from “the best of both worlds”. To this end, we explore a duo space (i.e., BEV and PV) 3D perception framework, in conjunction with some useful duo space fusion strategies that allow effective aggregation of the two feature representations.

Our proposed method, DuoSpaceNet, leverages two distinct feature spaces and achieves the state-of-the-art 3D object detection and BEV map segmentation results on nuScenes dataset.

1. Introduction

3D detection and segmentation via multi-view images undergoes active research [14, 22, 31, 38] due to its usefulness in applications like autonomous driving, where it can enhance downstream tasks such as object tracking [13, 34] and motion prediction [3, 44]. While there are many LiDAR-based 3D detection and segmentation methods which yield better results, camera-only methods still have their unique advantages. For example, camera-only perception systems are generally cost-friendly to deploy and have a higher resolution for distant objects.

Most existing methods [4, 14, 17, 22, 38] fall into one of the following two categories: bird’s-eye-view-based (BEV-based) methods or perspective-view-based (PV-based) methods, as depicted in Fig. 1. BEV-based methods [4, 14] spend great efforts on generating a bird’s-eye-view (BEV) feature map via a 2D to 3D lifting strategy, usually based on camera projection or unprojection model.

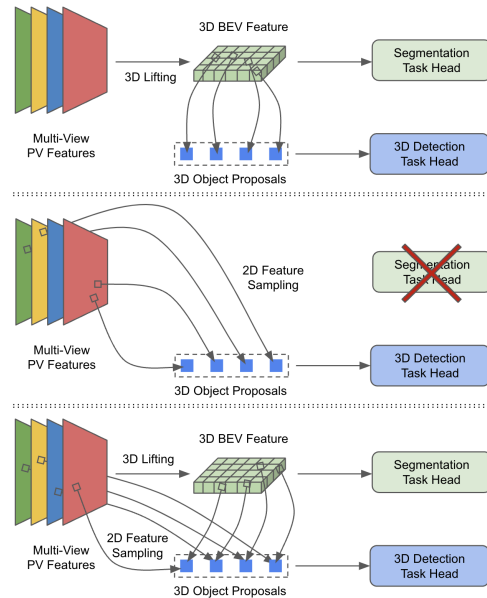


Figure 1. Comparison of different image-only 3D perception frameworks. **(a) Top:** Bird’s-eye-view-based (BEV-based) methods **(b) Middle:** Perspective-view-based (PV-based) 3D detection-only methods **(c) Bottom:** DuoSpaceNet (ours) where 3D detection benefits from both 3D BEV and 2D PV feature space. Dense segmentation is also doable.

Each element in the BEV feature map corresponds to the feature of a mapped 3D location. Subsequent detection and segmentation tasks are performed directly in BEV feature space. PV-based 3D detection methods [17, 38], however, directly build their detection heads on top of 2D image features. These methods generally utilize a handful of sparse detection proposals, often in the hundreds. For 3D detection, visual cues are directly gathered from sparse locations on PV image features where the proposals are anchored at. PV-based methods are specialized for object detection and they are more computationally efficient in general.

While both BEV-based methods and PV-based methods seem to work well, some of their shortcomings are outstand-

* Equal contribution.

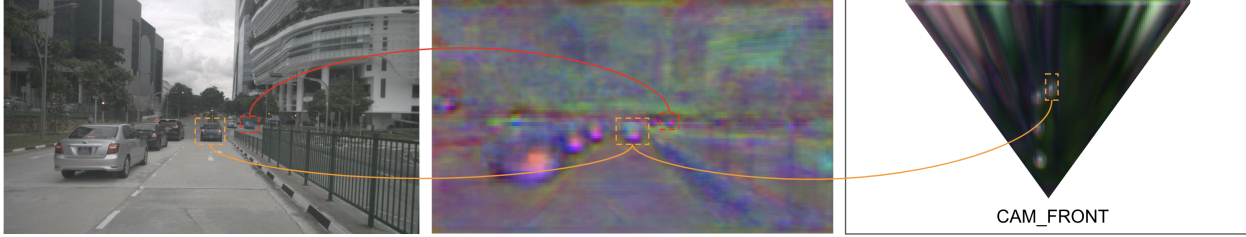


Figure 2. Example of differences between bird’s-eye-view (BEV) features and perspective view (PV) features. **(a) Left:** The original front-facing RGB image. **(b) Middle:** PV heat map. **(c) Right:** BEV heat map. Both heat maps are produced by our final model. Different hues and brightness represent different responses. Black represents low or no response. We find that each feature space has its own strengths. In this example, it is easier to reason object positions (e.g., the relative positions to the leading vehicles in **orange** dashed boxes) by looking into the BEV heat map. Meanwhile, none of the vehicle responses in BEV space overlap. When it comes to the PV heat map, more detailed semantics are preserved with a higher resolution, making it more desired for object attribute prediction. More importantly, it also shows response for objects outside BEV feature map range (e.g., vehicle in **red** dashed boxes), making far range object detection possible.

ing. When it comes to BEV-based methods, since multi-view pose parameters guide the feature lifting process, BEV features tend to have a better understanding of the underlying 3D geometry of a scene, which is crucial for estimating the 3D position of an object. BEV features are more robust to object scale variations and are free from overlap issues caused by perspective projection. However, subtle visual cues may be compromised due to coarse grid granularity, downsampling or interpolation. Additionally, because of the fixed-size nature of the BEV feature map, objects beyond the pre-set BEV range are destined to be disregarded, even if they possess a very large speed and will interact with the autonomous vehicle shortly. In contrast, PV-based methods seem to maximize the efficiency for 3D object detection by attending to 2D PV features sparsely and are capable of detecting objects at any distance theoretically. However, they lack certain functionalities and extensibilities such as handling map segmentation as well as multi-modal inputs. Moreover, they also tend to exhibit inferior 3D perception performance compared to BEV-based methods, as 3D information can only be implicitly inferred from PV features.

Take Fig. 2 as an instance, it is apparently more difficult to retrieve 3D spatial clues from the PV than the BEV feature map. Moreover, being perspective, the PV feature map suffers from occlusion and perspective distortion, whereas we can have an unobstructed and rectified view of objects in BEV space. However, BEV feature maps lack fine-grained details, especially for small objects such as pedestrian and cyclist due to resolution. It also affected by camera ray-like artifacts from back-projection and limited perception range due to fixed-size BEV range, whereas PV features are free from these issues.

Based on the above reasonings, BEV-based and PV-based methods are rather complementary. By combining them, we benefit from the rich geometric information provided by the BEV space within the fixed BEV feature map range. At the same time, thanks to PV feature maps, the ability to detect objects at far ranges can be maintained. In

order to bridge the gap between current BEV-based and PV-based frameworks to preserve “the best of both worlds”, in this paper, we propose DuoSpaceNet, a new paradigm that jointly tackles 3D object detection and map segmentation tasks via both BEV and PV feature representations. In our network, both PV features and BEV features are retained and fed into our Duo Space Decoder for object detection, a variant of the transformer decoder used in Deformable DETR [47]. To maintain the uniqueness of each feature space while creating a unified representation for individual 3D object, each object query comprises duo space content embeddings from both PV and BEV spaces, alongside a shared pose embedding that represents its real-world 3D pose. The decoder incorporates space-specific cross-attention layers to refine the duo space object queries using features from both spaces. To maximize the distinctiveness between BEV and PV features, feature divergence enhancement is introduced as the finishing touch of our BEV feature generation process. A temporal version of DuoSpaceNet is also established to show our framework’s adaptability from single to multiple frames. To achieve this, we propose a unique duo space temporal solution which elegantly processes temporal inputs via duo space temporal queries. For map segmentation, we append a convolution-based segmentation heads after BEV feature generation, and predict each map category separately.

In short, our novelties and contributions are as follows:

- We recognize and leverage the complementary strengths of feature modeling in bird’s-eye-view (BEV) space and perspective view (PV) space. Our proposed model, DuoSpaceNet, performs 3D detection using a novel multi-feature-space paradigm designed to maximize the potential of both feature spaces.
- To accomplish our duo space framework, we propose: 1) a *duo space decoder* for duo space feature extraction and fusion; 2) a *divergence feature enhancement* design to increase inter-space distinctiveness; and 3) a *duo space temporal modeling* method to extend our paradigm to a multi-frame setting.

- On nuScenes dataset [1], we conduct extensive experiments and ablation studies to verify the performance and effectiveness of our proposed ideas. We are able to demonstrate that DuoSpaceNet achieves the state-of-the-art results on both 3D object detection and map segmentation benchmarks, as well as the necessity of each individual design that we propose.

2. Related Work

2.1. BEV-Based Multi-View 3D Perception

Tackling multi-view 3D object detection task by bird’s-eye-view (BEV) representations has been a popular trend in autonomous driving industry. Following LSS [30], BEVDet [7, 8] and BEVDepth [12] unproject 2D image features into an explicit BEV feature map using dense depth predictions. M²BEV [41] and SimpleBEV [5] improve the efficiency of 2D to 3D BEV transformation by assuming a uniform distribution of depths when doing camera back-projection. Surprisingly, BEV-based methods can work without the non-trivial dense depth estimation. BEVFormer series [14, 31, 43] model dense BEV feature map with per-dataset queries optimized via deformable attention [47]. BEVFormer v2 [43] adds a perspective 3D detection head as an auxiliary task, but it does not fully capitalize on the potential of both feature spaces. OCBEV [31] introduces object aligned temporal fusion module to focus on instance-level temporal modeling. Going on, most recent BEV-based 3D detection methods [4, 28, 29, 48] shift their endeavors to improve temporal designs rather than fundamentals of BEV feature representations.

Another focus of BEV-based 3D perception is to handle the map segmentation task. Early works [25, 27, 30] tend to treat it as an individual task, while recent works, such as M²BEV and BEVFormer, explore the potential of jointly tackling object detection and map segmentation tasks by multi-task learning.

2.2. PV-Based Multi-View 3D Perception

Starting with DETR3D [38], the landscape of multi-view perspective-view-based (PV-based) 3D object detection leans towards sparse query refinement with set-to-set matching loss. Following studies like PETR [21, 22] and CAPE [42] improve transformer-based detection decoders with 3D position-aware image features. Recently, Sparse4D [17] further extends this track with the introduction of 4D anchors, allowing intuitive ego-motion and object motion compensation. We also find it useful and derive our query design from it. Similar to the BEV-based 3D detection track, current state-of-the-art PV-based methods, such as [18, 19, 37], also focus on improving temporal modeling techniques by temporal query propagation.

3. Method

As shown in Fig. 3, in our framework, PV and BEV feature maps are firstly generated from multi-view images and are then fed into the duo space decoder for object detection. The object queries equipped with duo space embedding are updated layer-by-layer in the decoder and the outputs from the last layer are used for predicting object labels and 3D poses. In addition, a dense segmentation head is built upon the BEV feature map for map segmentation.

3.1. Duo Space Features

Feature extraction. Multi-view images are first processed by an image encoder, which includes a backbone network (e.g., ResNet [6]) and a neck (e.g., FPN [15]), to generate multi-scale PV features $\{F_{PV}^j \in \mathbb{R}^{N \times C_j \times H_j \times W_j}, j = 1, 2, \dots, M\}$, where N, M are the number of cameras and different scales, H_j, W_j, C_j denote the feature map height, width and channel number of the j -th scale. Multi-view multi-scale PV features are lifted from 2D to 3D via a simple parameter-free back-projection module following previous work [5]. A 3D volume of coordinates with size $X \times Y \times Z$ is first generated and projected onto multiple images. PV features sampled around the projected positions are then aggregated by bilinear interpolation, resulting in a voxel feature map $F_{voxel} \in \mathbb{R}^{C \times X \times Y \times Z}$, where X, Y, Z, C represent the size of the voxel space and channels of the voxel feature. Eventually, the Z dimension is reduced to yield a BEV feature map $F_{BEV} \in \mathbb{R}^{C \times X \times Y}$.

In multi-frame settings, historical images are processed by the same procedure sequentially, generating PV and BEV feature maps for different frames. Both feature maps within a fixed temporal length are stored for future use.

Feature divergence enhancement. Our model benefits from the contrastiveness between the two feature representations. Since our lifting method is parameter-free, its functionality can be viewed as rearranging PV features given priors (e.g., camera poses) on the 3D geometry of a scene. Therefore, it has minimal effects on diverging the feature contents. To increase the heterogeneity of BEV features w.r.t. PV features, we propose a simple yet effective divergence enhancement stage. It consists of three 3D convolution layers (Conv3Ds) and three 2D convolution layers (Conv2Ds). First, we apply Conv3Ds on F_{voxel} to improve 3D geometry awareness in a learning-based fashion. After F_{voxel} is flattened along its Z dimension, Conv2Ds are applied for further BEV-level refinement, yielding final F_{BEV} .

3.2. Duo Space Decoder

Duo space queries. Suppose we have k object queries, $\{Q^i\}_{i=1}^k$. Each consists of a pose embedding, Q_{Pose}^i , and duo space content embedding for both BEV and PV spaces,

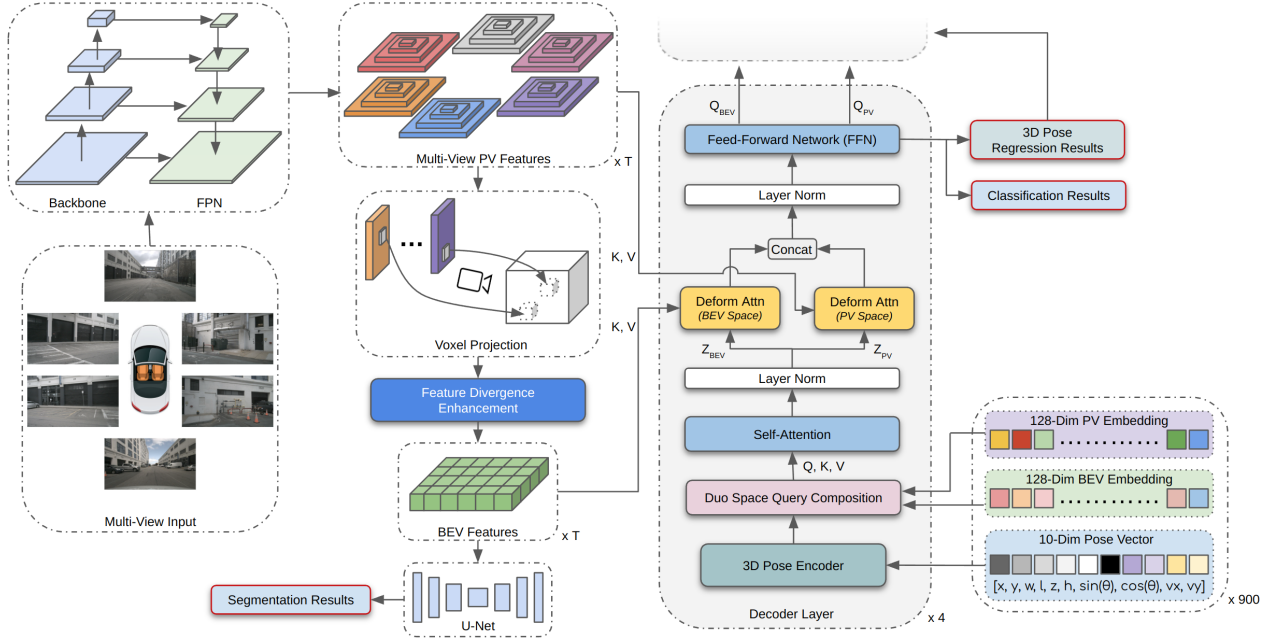


Figure 3. Overall architecture of the proposed DuoSpaceNet. Multi-view 2D perspective view (PV) features are extracted by the backbone and the feature pyramid network (FPN) [15]. Our 2D to 3D BEV lifting strategy consists of a parameter-free voxel projection following [5] and a divergence enhancement process to make resulting BEV features more distinctive w.r.t. PV features. In our duo space framework, multi-view PV features and BEV features are identified as equally important and are fed into the decoder together. Each decoder layer has one self-attention layer and two deformable cross-attention layers [47]. The self-attention layer acts on both BEV and PV spaces, whereas each cross-attention layer only attends to either BEV features or PV features. This space-specific cross-attention helps preserve the uniqueness of different feature spaces throughout multi-layer refinement process. Details about the Duo Space Query Composition can be found in Eqs. (2) to (4). Dense map segmentation can be jointly carried out via a separate segmentation head.

Q_{BEV}^i and Q_{PV}^i , respectively. Adapted from [17], each Q_{Pose}^i is encoded from a 3D pose vector \mathcal{P}_i , which contains attributes with physical meanings, including x, y, z in the vehicle coordinate system, the width, length, height, orientation and the velocity of the object the query is associated with. While Q_{BEV}^i and Q_{PV}^i contain high-level content features in BEV space and PV space respectively. In each layer of the duo space decoder, first, a pose encoder consisting of several FC layers is used to encode $\{\mathcal{P}_i\}_{i=1}^k$ into high dimensional latent representations, dubbed $\{\text{Enc}(\mathcal{P}_i)\}_{i=1}^k$, which will serve as learnable positional encodings in the subsequent attention layers. To unify the 3D pose of each object query across BEV and PV spaces, we generate a shared pose embedding,

$$Q_{Pose}^i = \xi(\text{Enc}(\mathcal{P}_i)), i \in \{1, 2, \dots, k\}, \quad (1)$$

where $\xi(\cdot)$ denotes a linear transformation to make the dimension of $\text{Enc}(\mathcal{P}_i)$ the same as Q_{BEV}^i and Q_{PV}^i . The final duo space queries in BEV space and PV space can be derived by simply adding the corresponding content embedding with the shared pose embedding together by

$$\mathbf{z}_{BEV} = \{Q_{BEV}^i + Q_{Pose}^i\}_{i=1}^k, \quad (2)$$

$$\mathbf{z}_{PV} = \{Q_{PV}^i + Q_{Pose}^i\}_{i=1}^k. \quad (3)$$

The self-attention layer thus can be represented as

$$Q = K = V = \mathbf{z}_{BEV} \oplus \mathbf{z}_{PV}, \quad (4)$$

$$\text{MHSA}(Q, K, V) = \text{Softmax}\left(\frac{QK^T}{\sqrt{\dim(K)}}\right)V, \quad (5)$$

where \oplus denotes a concatenation operator along the channel dimension and $\text{MHSA}(\dots)$ stands for multi-head self-attention described in [35].

Space-specific cross-attention. For multi-head cross-attention layers $\text{MHCA}_{BEV}(\dots)$ and $\text{MHCA}_{PV}(\dots)$, each of them will only act on their corresponding features using corresponding inputs. In BEV space, it can be represented as

$$\hat{\mathbf{P}}_{BEV} = \{\mathcal{P}_i|_{x,y}\}_{i=1}^k, \quad (6)$$

$$\text{MHCA}_{BEV}(\dots) = \text{MSDA}(\mathbf{z}_{BEV}, \hat{\mathbf{P}}_{BEV}, F_{BEV}), \quad (7)$$

where $\hat{\mathbf{P}}_{BEV}$ denotes the normalized coordinates of 3D reference points (only using their X and Y components here). $\text{MSDA}(\dots)$ is the Multi-Scale Deformable Attention Module (MSDeformAttn) described in [47]. Similarly, we have cross-attention in PV space as

$$\hat{\mathbf{P}}_{PV} = \{\text{Proj}(\mathcal{P}_i|_{x,y,z}, \{\mathbf{K}_n, \mathbf{T}_n\}_{n=1}^N)\}_{i=1}^k, \quad (8)$$

$$\text{MHCA}_{PV}(\dots) = \text{MSDA}(\mathbf{z}_{PV}, \hat{\mathbf{P}}_{PV}, \{F_{PV}^j\}_{j=1}^M), \quad (9)$$

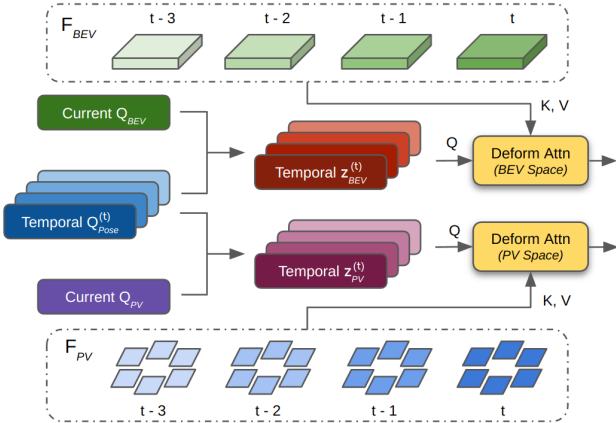


Figure 4. Diagram of the proposed duo space temporal modeling with 4 frames. Temporal pose embeddings $Q_{Pose}^{(t)}$ are generated by warping pose vectors at current timestamp through motion compensation. Subsequently, temporal duo space queries $z_{BEV}^{(t)}$ and $z_{PV}^{(t)}$ are assembled by broadcasting current content embeddings over the time dimension and then combining them with the temporal pose embeddings. We then conduct space-specific cross-attention using recent BEV and PV feature maps, both of which are maintained by their respective memory queue. Note that temporal queries from each timestamp only interact with feature maps corresponding to that timestamp. The resulting temporal queries are aggregated via a MLP in a recurrent fashion.

where $\text{Proj}(\dots)$ refers to the projection of 3D LiDAR coordinates into 2D image frames using camera matrices $\{\mathbf{K}_n\}_{n=1}^N \subset \mathbb{R}^{3 \times 3}$ and $\{\mathbf{T}_n\}_{n=1}^N \subset \mathbb{R}^{4 \times 4}$. Since this attention happens in PV space, multi-scale PV features $\{F_{PV}^j\}_{j=1}^M$ are used. Following feature extraction and refinement through multi-head space-specific cross-attention layers, the outputs of MHCA_{BEV} and MHCA_{PV} are concatenated as refined object queries, which are then fed into a 2-layer feed forward network (FFN). Finally, the FFN outputs are used for object category prediction and are also decoded into a 10-dim 3D pose vector as our detection regression results. The refined poses then serve as inputs for subsequent decoder layers.

3.3. Duo Space Temporal Modeling

BEV-based 3D detection methods [7, 14] typically utilize temporal inputs by stacking temporal BEV feature maps. Offsets are determined either with motion compensation or in a learnable manner (e.g., deformable attention) or both combined. Meanwhile, PV-based methods [17, 22] generally infuse temporal information into object queries. Therefore, the difference between BEV-based and PV-based temporal methods brings challenges to temporal design in our duo space paradigm. In this section, we present a unified temporal solution for both spaces via temporal duo space queries, illustrated in Fig. 4. Concretely, for a fixed temporal length l , each object is represented by l temporal duo space queries, each comprising a temporal pose of the underlying object and a shared content embedding. Temporal poses are deduced by applying both ego- and object-

motion compensation on the object’s current pose vector. The queries are fed into the space-specific cross-attention layer corresponding to their space. Each query only attends to features from a specific timestamp associated with its temporal pose. Subsequently, results produced by l temporal queries are recurrently aggregated via multi-layer perceptron (MLP) into a single refined prediction per object. Our solution elegantly operates symmetrically across BEV and PV spaces. Please refer to the supplementary materials for more details.

3.4. Multi-Task Learning

Similar to BEV-based methods, our model is capable of joint optimization of detection and segmentation. To perform dense segmentation, we simply add a segmentation branch consisting of a U-Net [32] like structure for feature enhancement and two parallel convolution-based segmentation heads for final predictions. It takes the BEV feature map F_{BEV} as input, and outputs two segmentation masks of the same resolution. To supervise the map segmentation branch, we use a weighted sum of focal loss [16] and dice loss [26] during training.

4. Experiments

Dataset. We benchmark our method on nuScenes dataset [1], one of the most widely-used public datasets in autonomous driving. The nuScenes dataset consists of 1,000 driving video clips. Each clip is 20-second long at the sampling frequency of 2Hz. Across the dataset, image data come from the same 6-camera setup, facing at 6 directions, providing a full 360° panoramic view. For 3D object detection task, the dataset contains 10 commonly-seen classes (e.g., car, pedestrian), in total $\sim 1.4\text{M}$ bounding boxes. We evaluate our 3D detection results using official nuScenes metrics, including mean average precision (mAP), nuScenes detection score (NDS), mean average error of translation (mATE), scale (mASE), orientation (mAOE), velocity (mAVE) and attribute (mAAE). For map segmentation, we follow previous works [30, 41] and evaluate our method with intersection of union (IoU) metric.

Implementation details. For both single-frame and multi-frame 3D detection experiments, if not specified otherwise, we completely follow the hyperparameter settings in [17], including the learning rate and its schedule, data augmentation, loss functions and anchor initialization. For full model experiments, the BEV feature map is sized 200×200 , the number of duo space queries is 900 and the number of decoder layers is 4. All layers have identical settings with 8 attention heads in both self-attention and cross attention layers. For deformable cross attention layers, we compute 16 offsets per query. For multi-frame experiments, we use 4 adjacent frames (including the current frame) as temporal input. For all ablation studies, we use ResNet-50 [6],

Method	Venue	Image Size	Frames	mAP \uparrow	NDS \uparrow	mATE \downarrow	mASE \downarrow	mAOE \downarrow	mAVE \downarrow	mAAE \downarrow
DETR3D [38]	CoRL2022	1600 \times 900	1	0.349	0.434	0.716	0.268	0.379	0.842	0.200
PETR [21]	ECCV2022	1600 \times 900	1	0.370	0.442	0.711	0.267	0.383	0.865	0.201
BEVFormer-S [14]	ECCV2022	1600 \times 900	1	0.375	0.448	0.725	0.272	0.391	0.802	0.200
Sparse4D [17]	arXiv2022	1600 \times 640	1	0.382	0.451	0.710	0.279	0.411	0.806	0.196
SimMOD [45]	AAAI2023	1600 \times 900	1	0.366	0.455	0.698	0.264	0.340	0.784	0.197
CAPE [42]	CVPR2023	1600 \times 900	1	0.388	0.463	-	-	-	-	-
DuoSpaceNet (Ours)	-	1600 \times 640	1	0.399	0.462	0.683	0.279	0.376	0.829	0.205
UVTR [11]	NeurIPS2022	1600 \times 900	6	0.379	0.483	0.731	0.267	0.350	0.510	0.200
BEVFormer [14]	ECCV2022	1600 \times 900	4	0.416	0.517	0.673	0.274	0.372	0.394	0.198
PETRv2 [22]	ICCV2023	1600 \times 640	6	0.421	0.524	0.681	0.267	0.357	0.377	0.186
Sparse4D [17]	arXiv2022	1600 \times 640	4	0.436	0.541	0.633	0.279	0.363	0.317	0.177
OCBEV [31]	3DV2024	1600 \times 900	4	0.417	0.532	0.629	0.273	0.339	0.342	0.187
CAPE-T [42]	CVPR2023	1600 \times 640	2	0.431	0.533	-	-	-	-	-
DFA3D-MvACon [20]	CVPR2024	1600 \times 900	4	0.432	0.535	0.664	0.275	0.344	0.323	0.207
DuoSpaceNet (Ours)	-	1600 \times 640	4	0.443	0.547	0.603	0.275	0.360	0.314	0.195

Table 1. Comparison on 3D detection results on nuScenes val set. All methods are trained for 24 epochs using ResNet-101-DCN [46] and benefit from perspective view pre-training. Test time augmentation is not used for all experiments. Results not reported in the original paper are omitted.

Method	Space	Params	Flops	mAP \uparrow	NDS \uparrow
BEVDet	BEV	69.5M	1498.8G	0.339	0.389
BEVFormer-S	BEV	66.6M	1705.5G	0.375	0.448
Sparse4D _{T=1}	PV	58.3M	1453.8G	0.382	0.451
DuoSpaceNet	BEV+PV	64.8M	1771.7G	0.399	0.462

Table 2. Comparison on model complexity in terms of the number of parameters and the number of floating-point operations.

Method	Joint Training	IoU-Drivable \uparrow	IoU-Lane \uparrow
LSS	\times	72.9	20.0
M ² BEV	\checkmark	75.9	38.0
	\times	77.2	40.5
BEVFormer-S	\checkmark	77.6	19.8
	\times	80.7	21.3
DuoSpaceNet	\checkmark	80.8	45.9
(Ours)	\times	81.2	46.5

Table 3. Map segmentation on the nuScenes val set.

100 \times 100 BEV feature map (if applicable), 800 \times 320 input images and a 2-layer decoder, trained for 12 epochs. For map segmentation, we follow PETRv2 [22] to transform map layers from the global reference frame into the ego frame, and generate two 200 \times 200 ground truth segmentation masks for *drivable area* and *lane boundary* respectively.

4.1. 3D Object Detection Results

Our 3D detection results on nuScenes val set are shown in Tab. 1. Compared with other state-of-the-art single-/multi-frame methods, our method consistently outperforms others on mAP. Specifically, we achieve 1.7% mAP gain over the state-of-the-art PV-based method Sparse4D [17] and

2.4% mAP gain over the state-of-the-art BEV-based method BEVFormer-S [14], using the single-frame setup. The same is true for multi-frame results. Among all methods, DuoSpaceNet achieves the lowest mATE by a large margin, suggesting that our duo space design helps the model understand 3D scenes better. When it comes to other metrics, although our method does not achieve 1st place for some entries, we argue that on average our model surpasses others based on the NDS measurement. We also report our results on nuScenes test set in Tab. 4. Compared with PolarFormer-T [9], DuoSpaceNet achieves a considerable 1.2% mAP gain and 2.6% NDS gain. Note that different methods use different training strategy on the test set (e.g., longer training schedules, more temporal frames, etc.). Nonetheless, our model is capable of achieving competitive results against other state-of-the-art models.

We also compare our model complexity against other state-of-the-art BEV-only or PV-only methods using input images of size 1600 \times 640 under the single-frame setting. For all models, we test them on the same machine using DeepSpeed Flops Profiler¹. As shown in Tab. 2, under similar model sizes, DuoSpaceNet significantly outperforms BEVDet [8] and BEVFormer-S. It is also slightly better than Sparse4D, yet still capable of handling dense segmentation tasks.

4.2. Map Segmentation Results

In Tab. 3, we benchmark the map segmentation performance on nuScenes val set. All methods use ResNet-101-DCN backbone except for M²BEV, who has a more advanced backbone. Compared with previous methods, our model achieves the highest IoU for both *drivable area*

¹<https://www.deepspeed.ai/tutorials/flops-profiler/>

Method	Venue	Temporal	Image Size	mAP \uparrow	NDS \uparrow	mATE \downarrow	mASE \downarrow	mAOE \downarrow	mAVE \downarrow	mAAE \downarrow
DETR3D [38]	CoRL2022	\times	1600 \times 900	0.412	0.479	0.641	0.255	0.394	0.845	0.133
BEVDet [8]	arXiv2022	\times	1600 \times 900	0.424	0.488	0.524	0.242	0.373	0.950	0.148
BEVFormer-S [14]	ECCV2022	\times	1600 \times 900	0.435	0.495	0.589	0.254	0.402	0.842	0.131
PETR [21]	ECCV2022	\times	1408 \times 512	0.441	0.504	0.593	0.249	0.383	0.808	0.132
PolarFormer [9]	AAAI2023	\times	1600 \times 900	0.455	0.503	0.592	0.258	0.389	0.870	0.132
DuoSpaceNet (Ours)	-	\times	1600 \times 640	0.460	0.519	0.559	0.259	0.399	0.765	0.134
UVTR [11]	NeurIPS2022	\checkmark	1600 \times 900	0.472	0.551	0.577	0.253	0.391	0.508	0.123
BEVFormer [14]	ECCV2022	\checkmark	1600 \times 900	0.481	0.569	0.582	0.256	0.375	0.378	0.126
PETrv2 [22]	ICCV2023	\checkmark	1600 \times 640	0.490	0.582	0.561	0.243	0.361	0.343	0.120
PolarFormer-T [9]	AAAI2023	\checkmark	1600 \times 900	0.493	0.572	0.556	0.256	0.364	0.439	0.127
MV2D [39]	ICCV2023	\checkmark	1600 \times 900	0.511	0.596	0.525	0.243	0.357	0.357	0.120
Focal-PETR-T [36]	IV2023	\checkmark	1600 \times 640	0.511	0.592	0.546	0.243	0.373	0.357	0.115
DuoSpaceNet (Ours)	-	\checkmark	1600 \times 640	0.513	0.601	0.508	0.254	0.362	0.312	0.118

Table 4. Comparison on 3D detection results on nuScenes test set. All experiments are camera-only methods using pretrained V2-99 [10] backbone. Test time augmentation is not used for all experiments.

Method	w/ BEV	w/ PV	mAP \uparrow	NDS \uparrow
BEV Only	\checkmark		0.203	0.264
PV Only		\checkmark	0.212	0.261
Duo (Ours)	\checkmark	\checkmark	0.216	0.288

Table 5. Ablation of using duo space features.

Method	FDE	mAP \uparrow	NDS \uparrow
BEV Only	\checkmark	0.203	0.264
		0.210	0.260
Duo (Ours)	\checkmark	0.216	0.288
		0.229	0.294

Table 6. Ablation of the proposed feature divergence enhancement, dubbed ‘‘FDE’’ in the table header.

and lane boundary, regardless of whether the segmentation branch is trained jointly with object detection or not. While sharing modules between different tasks saves computational resources and reduces inference time, the jointly trained model does show a slight performance drop compared to the individually trained model on map segmentation. This phenomenon, known as the negative transfer effect, is consistent with findings from previous studies [14].

4.3. Ablation Studies

Duo Space Features. To demonstrate the advantages of using BEV and PV features together, we compare the model equipped with our proposed duo space object queries to two baselines where object queries solely attend to either BEV or PV features. As shown in Tab. 5, using features from both spaces leads to a 0.4% gain in mAP from the PV-only baseline and a considerable 2.4% gain in NDS from the BEV-only baseline.

Shared Pose	Shared Content	mAP \uparrow	NDS \uparrow
		0.202	0.252
\checkmark	\checkmark	0.225	0.290
\checkmark		0.229	0.294

Table 7. Ablation of the proposed Duo Space Queries.

BEV Temporal Method	mAP \uparrow	NDS \uparrow
Recurrent Stacking	0.236	0.337
Learnable Attention	0.243	0.340
Temporal Queries	0.266	0.385

Table 8. Ablation of different temporal strategies.

Feature Divergence Enhancement. To make BEV features more distinctive from PV features, we propose adding feature divergence enhancement (FDE) during BEV feature generation. As shown in Tab. 6, while adding it to the BEV-only baseline can improve mAP by 0.7%, it won’t yield any help on NDS. Adding FDE in conjunction with our duo space design, however, will significantly improve the mAP by 1.3% and NDS by 0.6%, benefiting from the contrastiveness added between BEV and PV features.

Duo Space Queries. Although using feature maps from both spaces inherently has advantages over from single space, optimal performance cannot be achieved without our delicately designed duo space object queries. To validate this, three models differing only in their decoders were obtained. The first model, ‘‘unshared pose and unshared content’’, divides classical object queries into two sets, each attending separately to either BEV or PV features in cross-attention layers. The second model, ‘‘shared pose and shared content’’, makes each classical object query sequentially pass through self-attention, PV and BEV cross-attention layers, thus sharing pose and content embedding

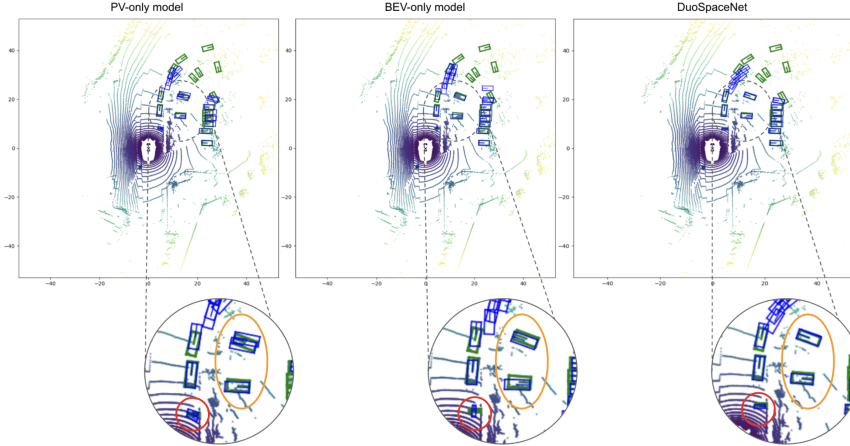


Figure 5. Visualization of 3D detection results in top-down view. Ground truth bounding boxes are in green and predictions are in blue. Please refer to the supplementary materials for the perspective camera view visualization.

across both spaces. The third model, “shared pose and un-shared content”, is equipped with our proposed duo space object queries. As Tab. 7 reveals, the first setting yields the worst result. In such a setting, each query only sees a single space of features, thereby losing the potential advantages offered by the presence of duo space features. The performance is marginally improved when pose and content embeddings are both shared, while the best results are achieved coupled with our Duo Space Decoder design. This implies that directly sharing content features across spaces might create latent space confusion due to different feature distributions. Decoupling content embeddings, however, proves to be more optimal by preserving unique feature representations from both spaces.

Temporal Modeling. We demonstrate the necessity of a unified temporal solution for both spaces in contrast to some trivial solutions. We keep using temporal queries in PV space across all experiments. In each experiment, we use a different temporal strategy in BEV space. Specifically, “Recurrent Stacking” refers to infusing temporal information by stacking up temporal BEV features. “Learnable Attention” refers to infusing temporal information by temporal self-attention proposed in BEVFormer. “Temporal Queries” refers to our method where both spaces infuse temporal information into their temporal duo space queries. As clearly shown in Tab. 8, temporal strategy matters a lot. The proposed Duo Space Temporal Modeling achieves far superior performance compared with simply using an off-the-shelf popular BEV temporal method in our duo space paradigm.

4.4. Qualitative Analysis

In addition to the quantitative analysis, we report qualitative results of our DuoSpaceNet in comparison with PV-only and BEV-only baselines. In this example, as top-down-view visualization (Fig. 5) reveals, the bounding boxes (high-

lighted by the orange ellipse) predicted by DuoSpaceNet align more closely with the ground truth in 3D space compared to the PV-only baseline. This alignment is attributed to the more explicit 3D spatial information in BEV features. Regarding the object pose estimation (the red circle in Fig. 5, depicting a motorcycle in the real world), due to the significant appearance information in PV features, both DuoSpaceNet and the PV-only baseline accurately predict its heading angle. In contrast, the BEV-only baseline provides an erroneous prediction differing by 90 degrees from the ground truth. Combined, we are confident that our duo space paradigm achieves “the best of both world”.

5. Conclusion and Discussion

In this paper, we introduce DuoSpaceNet, a camera-based 3D perception framework that aggregates information from both BEV and PV spaces. With our proposed duo space decoder design, our model is able to benefit from dense BEV representations and lossless PV features at the same time and achieve better performance on 3D object detection and map segmentation tasks. Ablation studies demonstrate the effectiveness of each individual design we propose, and extensive experiments on nuScenes dataset verify that our proposed DuoSpaceNet achieves competitive performance against state-of-the-art methods.

Limitation Though our framework is capable of long-range 3D detection compared to BEV-only methods, we cannot fully evaluate this capability on the nuScenes dataset due to the lack of far-range object ground truth data. In the future, we plan to conduct more comprehensive evaluations using larger datasets such as Argoverse2 [40]. Additionally, our current map segmentation task relies solely on the BEV feature map. We believe we can achieve better segmentation results, especially for detailed map structures, by combining PV features with BEV features in future research.

References

- [1] Holger Caesar, Varun Bankiti, Alex H Lang, Sourabh Vora, Venice Erin Liong, Qiang Xu, Anush Krishnan, Yu Pan, Giancarlo Baldan, and Oscar Beijbom. nuscenes: A multi-modal dataset for autonomous driving. In *Proceedings of the IEEE/CVF conference on computer vision and pattern recognition*, pages 11621–11631, 2020. 3, 5, 1
- [2] Nicolas Carion, Francisco Massa, Gabriel Synnaeve, Nicolas Usunier, Alexander Kirillov, and Sergey Zagoruyko. End-to-end object detection with transformers. In *European conference on computer vision*, pages 213–229. Springer, 2020. 1
- [3] Yiqian Gan, Hao Xiao, Yizhe Zhao, Ethan Zhang, Zhe Huang, Xin Ye, and Lingting Ge. Mgr: Multi-granular transformer for motion prediction with lidar. *arXiv preprint arXiv:2312.02409*, 2023. 1
- [4] Chunrui Han, Jianjian Sun, Zheng Ge, Jinrong Yang, Runpei Dong, Hongyu Zhou, Weixin Mao, Yuang Peng, and Xiangyu Zhang. Exploring recurrent long-term temporal fusion for multi-view 3d perception. *arXiv preprint arXiv:2303.05970*, 2023. 1, 3
- [5] Adam W. Harley, Zhaoyuan Fang, Jie Li, Rares Ambrus, and Katerina Fragkiadaki. Simple-BEV: What really matters for multi-sensor bev perception? In *IEEE International Conference on Robotics and Automation (ICRA)*, 2023. 3, 4
- [6] Kaiming He, Xiangyu Zhang, Shaoqing Ren, and Jian Sun. Deep residual learning for image recognition. In *Proceedings of the IEEE conference on computer vision and pattern recognition*, pages 770–778, 2016. 3, 5
- [7] Junjie Huang and Guan Huang. Bevdet4d: Exploit temporal cues in multi-camera 3d object detection. *arXiv preprint arXiv:2203.17054*, 2021. 3, 5
- [8] Junjie Huang, Guan Huang, Zheng Zhu, and Dalong Du. Bevdet: High-performance multi-camera 3d object detection in bird-eye-view. *arXiv preprint arXiv:2112.11790*, 2021. 3, 6, 7
- [9] Yanqin Jiang, Li Zhang, Zhenwei Miao, Xiatian Zhu, Jin Gao, Weiming Hu, and Yu-Gang Jiang. Polarformer: Multi-camera 3d object detection with polar transformer. In *Proceedings of the AAAI Conference on Artificial Intelligence*, pages 1042–1050, 2023. 6, 7
- [10] Youngwan Lee and Jongyoul Park. Centermask: Real-time anchor-free instance segmentation. In *Proceedings of the IEEE/CVF conference on computer vision and pattern recognition*, pages 13906–13915, 2020. 7
- [11] Yanwei Li, Yilun Chen, Xiaojuan Qi, Zeming Li, Jian Sun, and Jiaya Jia. Unifying voxel-based representation with transformer for 3d object detection. In *Advances in Neural Information Processing Systems*, pages 18442–18455. Curran Associates, Inc., 2022. 6, 7
- [12] Yinhao Li, Zheng Ge, Guanyi Yu, Jinrong Yang, Zengran Wang, Yukang Shi, Jianjian Sun, and Zeming Li. Bevdepth: Acquisition of reliable depth for multi-view 3d object detection. *Proceedings of the AAAI Conference on Artificial Intelligence*, 37(2):1477–1485, 2023. 3
- [13] Yanwei Li, Zhiding Yu, Jonah Philion, Anima Anandkumar, Sanja Fidler, Jiaya Jia, and Jose Alvarez. End-to-end 3d tracking with decoupled queries. In *Proceedings of the IEEE/CVF International Conference on Computer Vision*, pages 18302–18311, 2023. 1
- [14] Zhiqi Li, Wenhai Wang, Hongyang Li, Enze Xie, Chonghao Sima, Tong Lu, Qiao Yu, and Jifeng Dai. Bevformer: Learning bird’s-eye-view representation from multi-camera images via spatiotemporal transformers. *arXiv preprint arXiv:2203.17270*, 2022. 1, 3, 5, 6, 7
- [15] Tsung-Yi Lin, Piotr Dollár, Ross Girshick, Kaiming He, Bharath Hariharan, and Serge Belongie. Feature pyramid networks for object detection. In *Proceedings of the IEEE conference on computer vision and pattern recognition*, pages 2117–2125, 2017. 3, 4
- [16] Tsung-Yi Lin, Priya Goyal, Ross Girshick, Kaiming He, and Piotr Dollár. Focal loss for dense object detection. In *Proceedings of the IEEE international conference on computer vision*, pages 2980–2988, 2017. 5, 1
- [17] Xuewu Lin, Tianwei Lin, Zixiang Pei, Lichao Huang, and Zhizhong Su. Sparse4d: Multi-view 3d object detection with sparse spatial-temporal fusion. *arXiv preprint arXiv:2211.10581*, 2022. 1, 3, 4, 5, 6
- [18] Xuewu Lin, Tianwei Lin, Zixiang Pei, Lichao Huang, and Zhizhong Su. Sparse4d v2: Recurrent temporal fusion with sparse model. *arXiv preprint arXiv:2305.14018*, 2023. 3
- [19] Haisong Liu, Yao Teng, Tao Lu, Haiguang Wang, and Limin Wang. Sparsebev: High-performance sparse 3d object detection from multi-camera videos. In *Proceedings of the IEEE/CVF International Conference on Computer Vision*, pages 18580–18590, 2023. 3
- [20] Xianpeng Liu, Ce Zheng, Ming Qian, Nan Xue, Chen Chen, Zhebin Zhang, Chen Li, and Tianfu Wu. Multi-view attentive contextualization for multi-view 3d object detection. In *Proceedings of the IEEE/CVF Conference on Computer Vision and Pattern Recognition*, pages 16688–16698, 2024. 6
- [21] Yingfei Liu, Tiancai Wang, Xiangyu Zhang, and Jian Sun. Petr: Position embedding transformation for multi-view 3d object detection. In *Computer Vision – ECCV 2022*, pages 531–548, Cham, 2022. Springer Nature Switzerland. 3, 6, 7
- [22] Yingfei Liu, Junjie Yan, Fan Jia, Shuailin Li, Aqi Gao, Tiancai Wang, and Xiangyu Zhang. Petr2: A unified framework for 3d perception from multi-camera images. In *Proceedings of the IEEE/CVF International Conference on Computer Vision (ICCV)*, pages 3262–3272, 2023. 1, 3, 5, 6, 7
- [23] Ilya Loshchilov and Frank Hutter. Sgdr: Stochastic gradient descent with warm restarts. *arXiv preprint arXiv:1608.03983*, 2016. 1
- [24] Ilya Loshchilov and Frank Hutter. Decoupled weight decay regularization. *arXiv preprint arXiv:1711.05101*, 2017. 1
- [25] Chenyang Lu, Marinus Jacobus Gerardus van de Molengraft, and Gijs Dubbelman. Monocular semantic occupancy grid mapping with convolutional variational encoder-decoder networks. *IEEE Robotics and Automation Letters*, 4(2):445–452, 2019. 3
- [26] Fausto Milletari, Nassir Navab, and Seyed-Ahmad Ahmadi. V-net: Fully convolutional neural networks for volumetric medical image segmentation, 2016. 5
- [27] Bowen Pan, Jiankai Sun, Ho Yin Tiga Leung, Alex Andonian, and Bolei Zhou. Cross-view semantic segmentation

- for sensing surroundings. *IEEE Robotics and Automation Letters*, 5(3):4867–4873, 2020. 3
- [28] Jinhyung Park, Chenfeng Xu, Shijia Yang, Kurt Keutzer, Kris Kitani, Masayoshi Tomizuka, and Wei Zhan. Time will tell: New outlooks and a baseline for temporal multi-view 3d object detection. *arXiv preprint arXiv:2210.02443*, 2022. 3
- [29] Jinhyung Park, Chenfeng Xu, Shijia Yang, Kurt Keutzer, Kris Kitani, Masayoshi Tomizuka, and Wei Zhan. Time will tell: New outlooks and a baseline for temporal multi-view 3d object detection. *arXiv preprint arXiv:2210.02443*, 2022. 3
- [30] Jonah Philion and Sanja Fidler. Lift, splat, shoot: Encoding images from arbitrary camera rigs by implicitly unprojecting to 3d. In *European Conference on Computer Vision*, pages 194–210. Springer, 2020. 3, 5
- [31] Zhangyang Qi, Jiaqi Wang, Xiaoyang Wu, and Hengshuang Zhao. Ocbev: Object-centric bev transformer for multi-view 3d object detection. In *2024 International Conference on 3D Vision (3DV)*, pages 1188–1197. IEEE, 2024. 1, 3, 6
- [32] Olaf Ronneberger, Philipp Fischer, and Thomas Brox. U-net: Convolutional networks for biomedical image segmentation, 2015. 5
- [33] Carole H Sudre, Wenqi Li, Tom Vercauteren, Sebastien Ourselin, and M Jorge Cardoso. Generalised dice overlap as a deep learning loss function for highly unbalanced segmentations. In *Deep Learning in Medical Image Analysis and Multimodal Learning for Clinical Decision Support: Third International Workshop, DLMIA 2017, and 7th International Workshop, ML-CDS 2017, Held in Conjunction with MICCAI 2017, Québec City, QC, Canada, September 14, Proceedings 3*, pages 240–248. Springer, 2017. 1
- [34] Zheng Tang, Gaoang Wang, Hao Xiao, Aotian Zheng, and Jenq-Neng Hwang. Single-camera and inter-camera vehicle tracking and 3d speed estimation based on fusion of visual and semantic features. In *Proceedings of the IEEE conference on computer vision and pattern recognition workshops*, pages 108–115, 2018. 1
- [35] Ashish Vaswani, Noam Shazeer, Niki Parmar, Jakob Uszkoreit, Llion Jones, Aidan N Gomez, Łukasz Kaiser, and Illia Polosukhin. Attention is all you need. *Advances in neural information processing systems*, 30, 2017. 4
- [36] Shihao Wang, Xiaohui Jiang, and Ying Li. Focal-petr: Embracing foreground for efficient multi-camera 3d object detection. *IEEE Transactions on Intelligent Vehicles*, 2023. 7
- [37] Shihao Wang, Yingfei Liu, Tiancai Wang, Ying Li, and Xiangyu Zhang. Exploring object-centric temporal modeling for efficient multi-view 3d object detection. In *Proceedings of the IEEE/CVF International Conference on Computer Vision (ICCV)*, pages 3621–3631, 2023. 3
- [38] Yue Wang, Guizilini Vitor Campagnolo, Tianyuan Zhang, Hang Zhao, and Justin Solomon. Detr3d: 3d object detection from multi-view images via 3d-to-2d queries. In *In Conference on Robot Learning*, pages 180–191, 2022. 1, 3, 6, 7
- [39] Zitian Wang, Zehao Huang, Jiahui Fu, Naiyan Wang, and Si Liu. Object as query: Lifting any 2d object detector to 3d detection. In *Proceedings of the IEEE/CVF International Conference on Computer Vision*, pages 3791–3800, 2023. 7
- [40] Benjamin Wilson, William Qi, Tanmay Agarwal, John Lambert, Jagjeet Singh, Siddhesh Khandelwal, Bowen Pan, Ratnesh Kumar, Andrew Hartnett, Jhony Kaesemodel Pontes, Deva Ramanan, Peter Carr, and James Hays. Argoverse 2: Next generation datasets for self-driving perception and forecasting. In *Proceedings of the Neural Information Processing Systems Track on Datasets and Benchmarks (NeurIPS Datasets and Benchmarks 2021)*, 2021. 8
- [41] Enze Xie, Zhiding Yu, Daquan Zhou, Jonah Philion, Anima Anandkumar, Sanja Fidler, Ping Luo, and Jose M. Alvarez. M²bev: Multi-camera joint 3d detection and segmentation with unified birds-eye view representation, 2022. 3, 5
- [42] Kaixin Xiong, Shi Gong, Xiaoqing Ye, Xiao Tan, Ji Wan, Errui Ding, Jingdong Wang, and Xiang Bai. Cape: Camera view position embedding for multi-view 3d object detection. In *Proceedings of the IEEE/CVF Conference on Computer Vision and Pattern Recognition (CVPR)*, pages 21570–21579, 2023. 3, 6
- [43] Chenyu Yang, Yuntao Chen, Hao Tian, Chenxin Tao, Xizhou Zhu, Zhaoxiang Zhang, Gao Huang, Hongyang Li, Yu Qiao, Lewei Lu, Jie Zhou, and Jifeng Dai. Bevformer v2: Adapting modern image backbones to bird’s-eye-view recognition via perspective supervision. In *Proceedings of the IEEE/CVF Conference on Computer Vision and Pattern Recognition (CVPR)*, pages 17830–17839, 2023. 3
- [44] Ethan Zhang, Hao Xiao, Yiqian Gan, and Lei Wang. Sapi: Surroundings-aware vehicle trajectory prediction at intersections. *arXiv preprint arXiv:2306.01812*, 2023. 1
- [45] Yunpeng Zhang, Wenzhao Zheng, Zheng Zhu, Guan Huang, Jiwen Lu, and Jie Zhou. A simple baseline for multi-camera 3d object detection. In *Proceedings of the AAAI Conference on Artificial Intelligence*, pages 3507–3515, 2023. 6
- [46] Xizhou Zhu, Han Hu, Stephen Lin, and Jifeng Dai. Deformable convnets v2: More deformable, better results, 2018. 6
- [47] Xizhou Zhu, Weijie Su, Lewei Lu, Bin Li, Xiaogang Wang, and Jifeng Dai. Deformable detr: Deformable transformers for end-to-end object detection. *arXiv preprint arXiv:2010.04159*, 2020. 2, 3, 4
- [48] Zhuofan Zong, Dongzhi Jiang, Guanglu Song, Zeyue Xue, Jingyong Su, Hongsheng Li, and Yu Liu. Temporal enhanced training of multi-view 3d object detector via historical object prediction. In *Proceedings of the IEEE/CVF International Conference on Computer Vision (ICCV)*, pages 3781–3790, 2023. 3

DuoSpaceNet: Leveraging Both Bird’s-Eye-View and Perspective View Representations for 3D Object Detection

Supplementary Material

6. Additional details on Duo Space Temporal Modeling.

Specifically, we generate temporal duo space queries $\mathbf{z}_{BEV}^{(t)}$ and $\mathbf{z}_{PV}^{(t)}$ by infusing past information into shared 3D poses. Assuming the current timestamp is T and the temporal length is l frames, we compute temporal poses $\mathcal{P}_i^{(t)}, i \in \{1, 2, \dots, k\}, t \in \{T - l + 1, T - l + 2, \dots, T\}$. Ego-motion compensation can be done via a warp transformation matrix from timestamp $t - 1$ to t , denoted as $[\mathbf{R} | \mathbf{t}]_{(t)}^{(t-1)}, t \in \{T - l + 1, T - l + 2, \dots, T\}$, where \mathbf{R} and \mathbf{t} refer to the rotational and translational components in the matrix. Object-motion compensation, on the other hand, can be tackled using the predicted velocity of each query, assuming a constant velocity motion model over the l -length sequence. Adding up both compensations, we update the object location x, y, z at $t - 1$, dubbed $\mathcal{P}_i^{(t-1)}|_{x,y,z}$, the object orientation $\sin \theta, \cos \theta$ at $t - 1$, dubbed $\mathcal{P}_i^{(t-1)}|_{\theta}$ and the object velocity v_x, v_y at $t - 1$, dubbed $\mathcal{P}_i^{(t-1)}|_{v_x,v_y}$, through

$$\mathcal{P}_i^{(t)}|_{x',y'} = \mathcal{P}_i^{(t)}|_{x,y} - \Delta t \cdot \mathcal{P}_i^{(t)}|_{v_x,v_y}, \quad (10)$$

$$\mathcal{P}_i^{(t-1)}|_{x,y,z} = [\mathbf{R} | \mathbf{t}]_{(t)}^{(t-1)} \mathcal{P}_i^{(t)}|_{x',y',z}, \quad (11)$$

$$\mathcal{P}_i^{(t-1)}|_{\theta} = \mathbf{R}_{(t)}^{(t-1)} \mathcal{P}_i^{(t)}|_{\theta}, \quad (12)$$

$$\mathcal{P}_i^{(t-1)}|_{v_x,v_y} = \mathbf{R}_{(t)}^{(t-1)} \mathcal{P}_i^{(t)}|_{v_x,v_y}, \quad (13)$$

$$i \in \{1, 2, \dots, k\}, t \in \{T - l + 1, T - l + 2, \dots, T\},$$

where Δt represents the wall-clock time difference between adjacent frames. We compute the temporal pose embedding for each timestamp t as follows:

$$(Q_{Pose}^i)^{(t)} = \xi \left(\text{ENC}(\mathcal{P}_i^{(t)}) \right). \quad (14)$$

We then generate $\mathbf{z}_{BEV}^{(t)}, \mathbf{z}_{PV}^{(t)}, \hat{\mathbf{p}}_{BEV}^{(t)}$ and $\hat{\mathbf{p}}_{PV}^{(t)}, t \in \{T - l + 1, T - l + 2, \dots, T\}$ according to Eq. 2, 3, 6 & 8 as temporal inputs. Finally, after cross-attention layers (Eq. 7 and 9), we aggregate temporal outputs via 3-layer MLP before the FFN of each decoder layer. An illustration of temporal cross-attention in PV space is shown in Fig. 6. The temporal cross-attention in BEV space is identical except for the use of BEV space queries and BEV features as input.

7. Additional details on experiment settings.

Following [17], we initialize the x, y, z coordinates of pose vectors using K-Means centroids on nuScenes training

set [1]. For all experiments, we use AdamW optimizer [24] and a cosine learning rate scheduler [23]. The initial learning rate for backbone and other modules are $2e-5$ and $2e-4$, respectively. No data augmentation is used other than the grid mask used in DETR3D [38]. The perception ranges for both the X and Y axes are $[-51.2m, 51.2m]$, which are consistent for both the 3D object detection and map segmentation tasks.

When it comes to the loss functions we use to train the 3D detection, we utilize Focal Loss [16] for bounding box classification and L1 Loss for attribute regression. Duo space queries are assigned to their ground truth via Hungarian Matching introduced in DETR [2]. For segmentation, we use a combination of L1 Loss, Cross Entropy Loss and Dice Loss [33] for each predicted mask.

8. Additional Visualizations

In Fig. 7, the 3D detection results are displayed in the perspective camera view for the same example as shown in Fig. 5, comparing three different detection methods along with the ground truth.

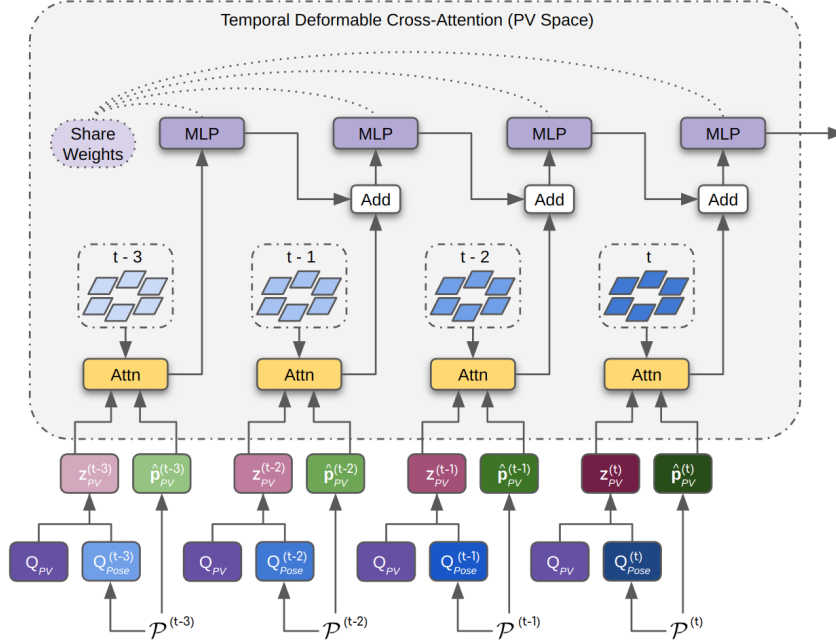


Figure 6. An illustration of space-specific temporal deformable cross-attention in perspective view (PV) space, with 4 temporal frames. Temporal pose vectors are generated by transforming current the pose vector at current frame to previous frames with motion compensation. After the duo space query composition, duo space temporal queries are formulated for both spaces. Subsequently, in PV space, attention queries, $z_{PV}^{(t)}$, and their reference points, $\hat{\mathcal{P}}_{PV}^{(t)}$, from timestamp $t-3$ to t are used as input queries for multi-scale deformable attention [47]. Each set of queries at a given timestamp only attends to corresponding PV features at the same timestamp. After the attention mechanism, results are aggregated by MLPs in a recurrent manner. Note that weights are shared across all MLPs.



Figure 7. Visualization of 3D detection results in perspective camera view. Different colors represent different categories.